Received: 1 March 2022 | Revised: 2 April 2022 | Accepted: 13 April 2022

DOI: 10.1002/cey2.224

RESEARCH ARTICLE

CARBON ENERGY WILEY

Localized-domains staging structure and evolution in lithiated graphite

Suting Weng[1,2] | **Siyuan Wu**[1,2] | **Zepeng Liu**[1,2] | **Gaojing Yang**[1,2] | **Xiaozhi Liu**[1] | **Xiao Zhang**[1,3] | **Chu Zhang**[1,3] | **Qiuyan Liu**[1,3] | **Yao Huang**[1,3] | **Yejing Li**[1] | **Mehmet N. Ateş**[4] | **Dong Su**[1] | **Lin Gu**[1] | **Hong Li**[1,5] | **Liquan Chen**[1] | **Ruijuan Xiao**[1,2] | **Zhaoxiang Wang**[1,2,3] | **Xuefeng Wang**[1,2,3,5]

[1]Beijing National Laboratory for Condensed Matter Physics, Institute of Physics, Chinese Academy of Sciences, Beijing, China

[2]School of Physical Sciences, University of Chinese Academy of Sciences, Beijing, China

[3]College of Materials Science and Opto-Electronic Technology, University of Chinese Academy of Sciences, Beijing, China

[4]Energy Storage Division, TÜBİTAK Rail Transport Technologies Institute, TÜBİTAK Gebze Campus, Gebze, Kocaeli, Turkey

[5]Tianmu Lake Institute of Advanced Energy Storage Technologies Co., Ltd., Liyang, Jiangsu, China

Correspondence
Xuefeng Wang, Ruijuan Xiao, and Zhaoxiang Wang, Beijing National Laboratory for Condensed Matter Physics, Institute of Physics, Chinese Academy of Sciences, 100190 Beijing, China.
Email: wxf@iphy.ac.cn; rjxiao@iphy.ac.cn and zxwang@iphy.ac.cn

Funding information
Natural Science Foundation of Beijing Municipality, Grant/Award Number: Z200013; National Natural Science Foundation of China, Grant/Award Numbers: 52172257, 22005334, 21773301, 52022106

Abstract

Intercalation provides to the host materials a means for controlled variation of many physical/chemical properties and dominates the reactions in metal-ion batteries. Of particular interest is the graphite intercalation compounds with intriguing staging structures, which however are still unclear, especially in their nanostructure and dynamic transition mechanism. Herein, the nature of the staging structure and evolution of the lithium (Li)-intercalated graphite was revealed by cryogenic-transmission electron microscopy and other methods at the nanoscale. The intercalated Li-ions distribute unevenly, generating local stress and dislocations in the graphitic structure. Each staging compound is found macroscopically ordered but microscopically inhomogeneous, exhibiting a localized-domains structural model. Our findings uncover the correlation between the long-range ordered structure and short-range domains, refresh the insights on the staging structure and transition of Li-intercalated/deintercalated graphite, and provide effective ways to enhance the reaction kinetic in rechargeable batteries by defect engineering.

KEYWORDS
cryogenic-transmission electron microscopy (cryo-TEM), graphite intercalation compounds, lithiated graphite, localized-domains structural model, staging structures

1 | INTRODUCTION

Ion intercalating into a host material provides a means to tune the physical/chemical properties over wide ranges.[1,2] Superconductivity was discovered in graphite intercalation compounds (GICs) with alkali metals while neither graphite nor alkali metals are superconductors.[3,4] Reversible intercalation and deintercalation of lithium (Li) into graphite initialized the golden era of Li-ion batteries and is still dominating the anode reaction without other comparable substitutes.[5] Although decades of efforts have been put into understanding and applying the intercalation chemistry of GICs,[6] many open questions remained unsolved or unclear, especially those associated with the nature of their staging structure and the kinetics of the stage formation and transitions, which hinders the further application of graphite at different operating conditions, such as fast charge.[7–9]

The staging intercalation is a general phenomenon that was observed in various cations or anions intercalated into layered materials,[10] such as Li^+ intercalating in $LiFePO_4$,[11] Na^+ inserting in MoS_2,[12] and $TFSI^-$ embedding in graphite.[13] As one of the characteristic features of GICs, the staging structure regulates the electronic structure of GICs and its dynamic evolution determinates the reaction rate of (de)intercalation for Li-ion batteries.[14–16] Two typical structural models were proposed to describe the possible micro-configuration of the staging structure but have not been evidenced (Figure 1A,B): Rüdorff-Hofmann (Figure 1A)[14] and Daumas-Hérold models (Figure 1B).[15] The former model (Figure 1A) believes that the Li ions alternatively occupy the interlayers for every four-to-one graphene layers in the Stage IV-to-I (LiC_{24}-to-LiC_6) but they are hard to transit smoothly, which indicates that fast charging of graphite is impossible due to the own kinetic limit.[17] The latter model (Figure 1B) assumes that deformation or rumpling of the graphene layer occurs during Li intercalation, which, in turn, facilitates the stage interconversion.[16] Both staging models show the same long-range-order structure but differ in the short-range domains, which requires microstructure-sensitive techniques to differentiate and uncover the true character of the staging structure.

Since graphite is a beam-sensitive material (Supporting Information: Figure S1), we carried out cryogenic-transmission electron microscopy (cryo-TEM) to inspect the microstructure of the Li-intercalating graphite at different stages in this study. Cryo-TEM is a powerful technique to minimize irradiation damage and maintain pristine structure and resolution.[18–20] The results show that the original graphite structure gradually becomes disordered during the lithiation process, forming dislocations and microdomains, which contain different staging structures. The deformation of graphene layers is caused by the local stress induced by the uneven Li distribution. Each staging structure is macroscopically ordered but microscopically inhomogeneous (Figure 1C). These structural defects and transitions are reversible during lithiation/delithiation of graphite. Our findings renew the micro configuration and transition of the staging structure and deepen the understanding of the intercalation chemistry.

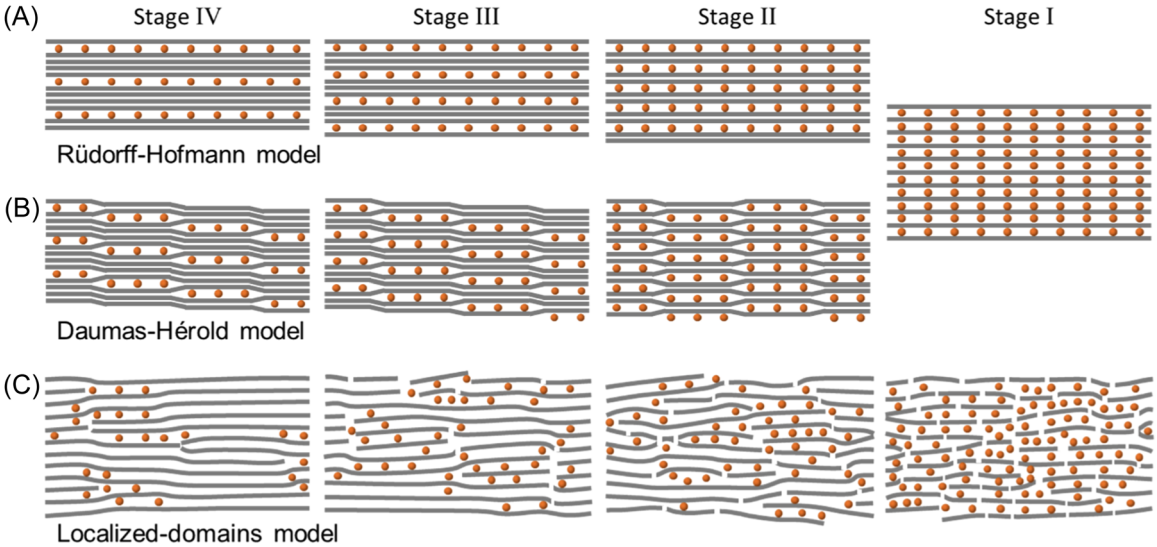

FIGURE 1 Schematic illustration of the lithiated graphite at different stages. (A) Rüdorff-Hofmann model. (B) Daumas-Hérold model. (C) Localized-domains model.

2 | EXPERIMENTAL SECTION

2.1 | Sample preparation process

The KOH etched graphite was synthesized from KS6 graphite (TIMCAL GRAPHITE & CARBON) by KOH etching.[21,22] Graphite (4 g) was stirred in the aqueous KOH solution (40 mL, 50 wt%) at 80°C for 24 h. The mixture was vacuum-filtered through a polytetrafluoroethylene (PTFE) membrane (Whatman) and then dried at 80°C for 12 h. The resultant powders were heat-treated at 400°C for 1 h in an argon gas-flowing tube furnace at the speed of 5 L min^{-1}. After heat treatment, the mixture was washed with distilled water until the pH of the filtrate reaches 7. The KOH-etched graphite was collected after drying.

The working electrode sheets were prepared by mixing the KS6 graphite powder and polyvinylidene fluoride dissolved in N-methyl pyrrolidone at a weight ratio of 9:1 and then casting the slurry onto a piece of copper foil. The foil was vacuum dried at 120°C for 6 h. The electrodes were punched with a diameter of 10 mm and areal loading of ~3.0 mg cm^{-2}. For in situ XRD samples, the working electrodes were prepared by mixing KS6 graphite powder and PTFE binder at a mass ratio of 95:5. The composites were ground to square thin slices with a width of 10 mm and an active loading amount of ~15 mg cm^{-2}, and then dried at 120°C under vacuum for 6 h.

Coin cells (CR2032) were assembled in an argon-filled glove box (MBraun Lab Master 130, H_2O and $O_2 < 0.1$ ppm), with the KS6 graphite as the working electrode, fresh lithium foil as the counter electrode, 1 mol L^{-1} lithium hexafluorophosphate ($LiPF_6$) dissolved in a mixture of ethylene carbonate (E and dimethyl carbonate (DMC) (1:1 volume/volume) as the electrolyte, and a polypropylene film (Celgard 2400) as the separator. The cells were galvanostatically cycled between 0.0 and 3.0 V at 20 mA g^{-1} to obtain the lithiated graphite at different stages on a Neware battery test system (CT-4008T-5V10mA-164; Shenzhen). The lithiated graphite electrodes were taken out of the cells, rinsed with DMC, and dried in the vacuum chamber of the glove box before the postmortem characterization.

2.2 | Characterization

The in situ powder X-ray diffraction (XRD) was performed on D8 Advance (Bruker) with monochromatic Cu Kα radiation ($\lambda = 1.541$ Å). The Raman spectra were recorded on a LabRAM HR Evolution Raman spectrometer (532 nm radiation; Horiba) with a resolution of 2 cm^{-1}. Cryo-TEM characterizations were carried out using a JEOL JEM-F200 microscope under cryogenic temperatures (−180°C) at 200 kV. Different lithiated graphite powder samples were scraped from the electrode sheets, rinsed by DMC, and then loaded on the TEM grids. It was transferred into the cryo-TEM holder (Fischione 2550) in an Ar-filled glove box and sealed inside of the holder. With an additional sealing container, the cryo-TEM holder was quickly inserted into the JEOL JEM-F200 microscope. Liquid nitrogen was added to the cryo-TEM holder and the sample temperature dropped and stabilized at −180°C. The structure of graphite and other species was analyzed using Digital Micrograph (DM; Gatan) software. Inverse fast Fourier transform (IFFT) was performed to improve the signal-to-noise ratio. Strain analysis was performed based on the geometric phase analysis (GPA) method[23] using the FRWR tools plugin (www.physics.hu-berlin.de/en/sem/software/software_frwrtools) in DM. ImageJ software was used to estimate the defect fraction by the area ratio of the weak contrast domains to the regular contrast domains.

2.3 | Simulation details

All the density functional theory (DFT) calculations were performed with the Vienna ab initio simulation package (VASP).[24] The projector-augmented wave approach[25] and the generalized gradient approximation Perdew–Burke–Ernzerhof[26] exchange and correlation functional were selected for all the calculations. The cutoffs for the wave function are 520 eV and the Gamma k-mesh used to sample the Brillouin zone is 6 × 6 × 6. Convergence was achieved until the total energy difference was less than 10^{-5} eV and the forcible convergence criterion was set as 0.01 eV $Å^{-1}$. The AIMD run was carried out with a Nose thermostat[27] for 1000 steps with a time step of 1 fs. The simulation temperature was set as 1000 and 1500 K for Li diffusion and structural evolution, respectively.

To check the stability of the phases, which may exist during the lithiation process, the formation energy of Li_xC_6 ($x = 0$, 1/4, 1/3, 1/2, and 1) was attained on the basis of the DFT calculations as the following equation:

$$\Delta E = E(Li_xC_6) - (1 - x)E(C_6) - xE(LiC_6), \quad (1)$$

where the $E(Li_xC_6)$, $E(C_6)$ and $E(LiC_6)$ denote the total energy of Li_xC_6, C_6, and LiC_6, respectively.

3 | RESULTS AND DISCUSSION

3.1 | Long-range structure of the lithiated graphite

Li ions were electrochemically intercalated into the graphite with a controlled concentration and rate.

Meantime, in situ X-ray diffraction (XRD) was applied to monitor the real-time structural changes of the graphite during the lithiation and delithiation process (Figure 2, Figure S2, and Figure S3). It demonstrates that graphite experiences a sequence of solid–solution phase transition from pristine graphite to the Stage IV (0.850–0.198 V), biphasic transition from Stage IV to Stage III (0.198–0.170 V), solid–solution phase transition during Stage III (0.170–0.110 V), biphasic transition from Stage III to Stage II (0.110–0.075 V), and biphasic transition from Stage II to Stage I (0.075–0 V), respectively. Two different staging phases coexist for more than half the period of the lithiation process. The lithiation of graphite starts at 0.850 V before which solid electrolyte interphase (SEI) forms as no visible bulk structural change was found in either XRD or TEM while some SEI inorganic species, such as LiF and Li_2O, were present on the surface of the graphite as observed by the cryo-TEM (Supporting Information: Figure S4). These structural changes are reversible when the graphite was delithiated as all the diffraction peaks are back to the original positions (Supporting Information: Figure S2).

3.2 | Local structure of the lithiated graphite by cryo-TEM

Because XRD is a technique sensitive to the long-range crystalline structure, cryo-TEM was performed as a complemental tool to probe the short-range local structure. As shown in Figure 3, the graphene layers in the pristine graphite are flat and orderly arranged (Figure 3A). There is a negligible change in the graphite bulk when it was discharged to 0.850 V (Figure 3B), before which side reactions occur to form SEI (Supporting Information: Figure S4). Li intercalating into graphite deforms the graphene layers, forming dislocations and other defects (Figure 3C–F). The extent of deformation is gradually increased with the continuous lithiation and its defect fraction (denoted as the area ratio of the defective domains to the whole observable part, Figure 3I and Figure S5) is estimated to be 27.1% (Figure 3C), 38.2% (Figure 3D), 55.3% (Figure 3E), and 70.2% (Figure 3F) in Stage IV, Stage III, Stage II, and Stage I structures, respectively.

When the graphite was delithiated, these defective domains are gradually reduced (Supporting Information: Figure 3G–H) and the stacking of graphene layers is back

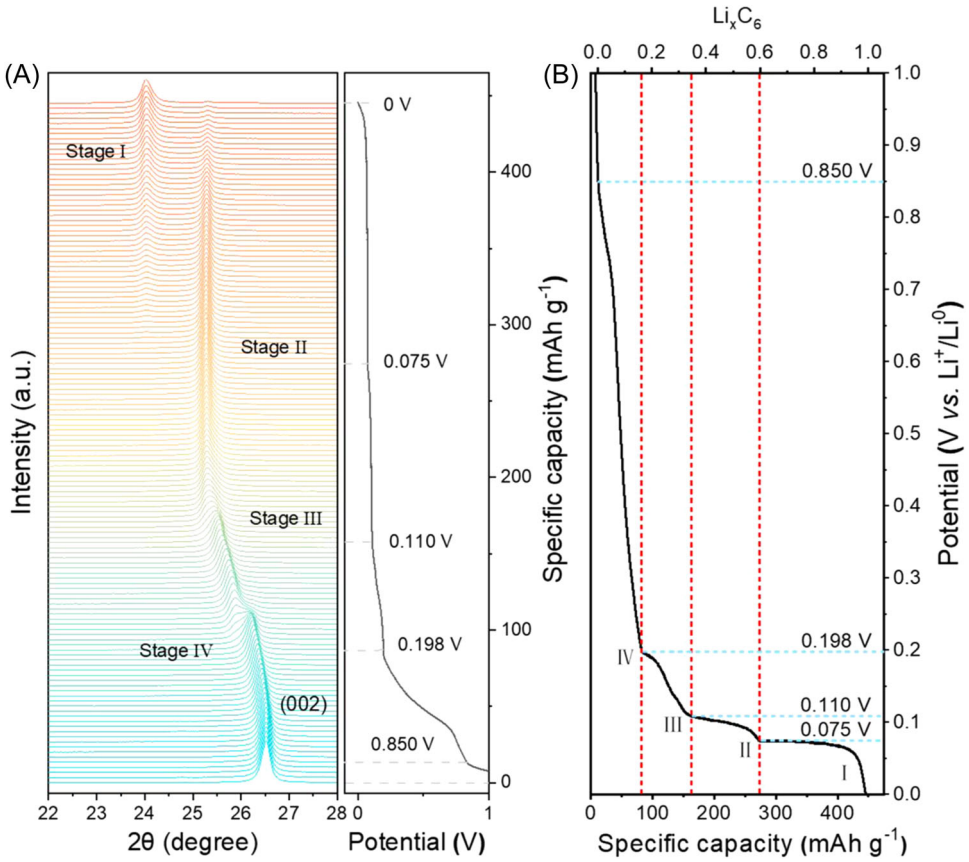

FIGURE 2 Long-range structural evolution of the graphite during electrochemical lithiation at a current density of 20 mA g^{-1}. (A) The in situ X-ray diffraction patterns recorded during lithiation. (B) The voltage curve of the graphite during lithiation.

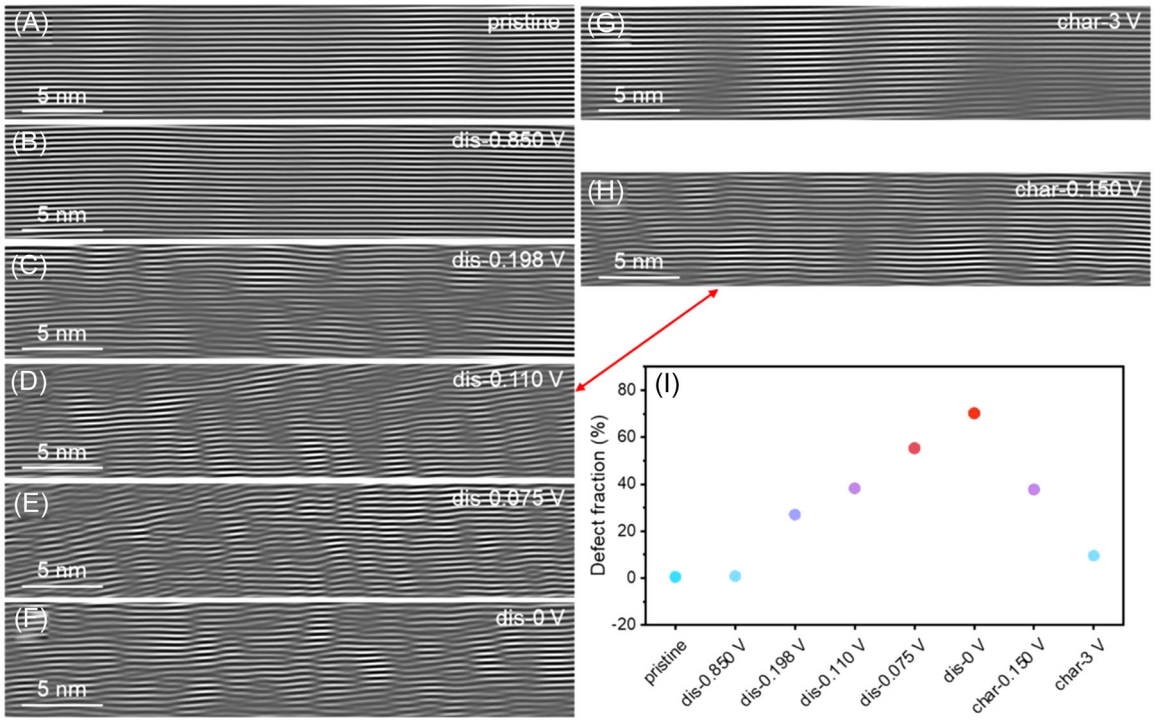

FIGURE 3 Local structural evolution of different graphite intercalation compounds. (A–H) Inverse fast Fourier transform images of graphite at different lithiation states. (I) Statistics of defective fraction in different lithiated graphite. char, charge; dis, discharge.

to the original state. It is worthy to note that Stage III at delithiation (charging to 0.150 V, Figure 3H) and lithiation (discharging to 0.110 V, Figure 3C) show a similar defective fraction, indicative of the high reversibility of phase transitions during lithiation and delithiation. When the graphite is charged to 3 V, most of the structure is recovered and the defective fraction is 9.6%, which may trap the Li ions and cause the irreversible capacity.

The deformed structure of graphite originated from the local stress induced by the Li-ion intercalation,[16] which is revealed by GPA (Figure 4 and Figures S6 and S7). Based on the distribution and interaction of the stress field, the observed defective structures can be classified into three types, as displayed in Figure 4A.

Defect I is an individual "Y"-like edge dislocation, which is caused by slipping the atomic plane by a half layer. It helps to transition from the multiple layers to the fewer layers (e.g., three-to-two layers [Defect i] and four-to-three layers [Defect ii]), where the former is compressed while the latter is tensed. As a result, a couple of compressive (in blue color) and tensive (in yellow color) strains are present in the stress field of Defect I.

Defect II consists of a pair of the Defect I with opposite Burgers vectors interacting at a certain distance. When two Defect I are close to each other, they are apt to attract, approach, and form a dislocation dipole (Defect II). This configuration is beneficial in reducing the total strain energy.[28] Especially, the preferential aggregation of interstitial atoms (in Defect v) or supersaturated vacancy (in Defect vi) in the crystal forms a Frank dislocation loop, which can move by atom diffusion.[29]

Defect III is a single strain region either in tension or in compression extended for a relatively large area (more than five layers), where displacement is less than half interlayer. It can be regarded as a start deformation of the graphene layers.

Statistical results (Figure 4B) show that these three defects are coexisting and their content varies among the different staged graphite, suggesting that they can be converted to each other during lithiation and delithiation. Note that the concentration of Defect III increases in Stage III at the lithiation (dis—0.110 V) and delithiation (char—0.150 V), indicating that more structural deformations are required to transition from Stage III to Stage II or Stage IV. Whereas, Defect I and II are dominated in the whole process, which facilitates the transition among different staging phases.

The strain maps in Figure 4C–G and Figure S7 demonstrate that the local stress field is prevalent in the lithiated graphite, which results in the redshift of the 2D band (2720 cm^{-1})[30] and the appearance of layer breathing modes (LBM, 112 and 128 cm^{-1})[31] in Raman spectra after lithiation (Supporting Information: Figure S8). Especially during phase transition from Stage III to Stage II, plenty of local stress is present and dispersed density (Figure 4E). These closely dispersed stress fields are

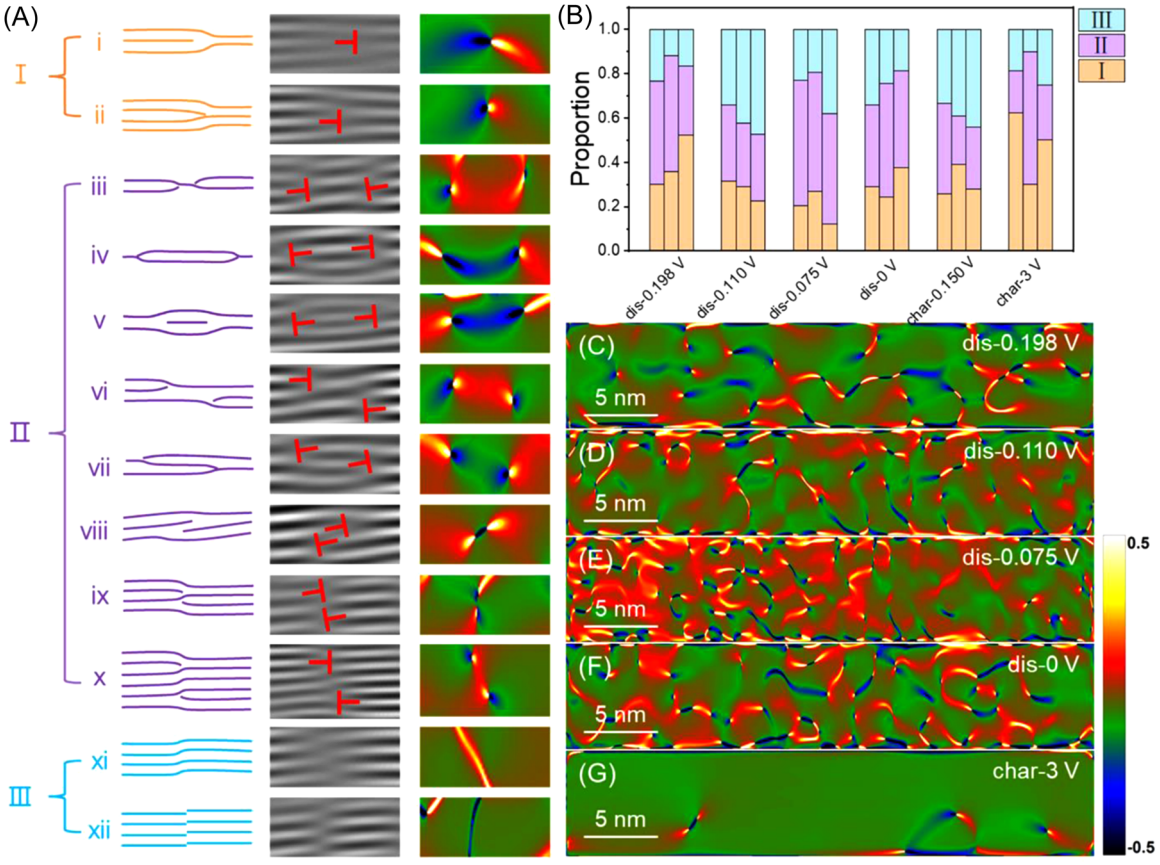

FIGURE 4 Defect classification and evolution in the lithiated graphite at different stages. (A) The schematics, transmission electron microscopy images, and the corresponding strain analysis of the defects. (B) Statistics results show the relative ratio among three defects. Strain maps of the lithiated graphite at the (C) 0.198 V, (D) 0.110 V, (E) 0.075 V, (F) 0 V, and charged to (G) 3 V. The color from red-to-yellow-to-white in the strain maps represents the gradually increased tensive strain while that from green-to-blue-to-black indicates the gradually enhanced compressive strain. char, charge; dis, discharge.

inclined to interact and merge, resulting in the reduced stress fields in Stage I (Figure 4F). When the Li ions are extracted from graphite, most of the stress fields disappear (Figure 4G), indicating the reversible generation and disappearance of the elastic stress field during the lithiation and delithiation of the graphite.

The long- and short-range structures of the lithiated graphite were further dug by measuring the d-spacings and indexing them based on the characteristic interplanar spacing of the specifically staged graphite (Figure 2 and Table S1). Figure 5 displays the microstructure of the lithiated graphite at different stages labeled with local (based on three to six graphene layers) and average interplanar spacing (based on 11 graphene layers). The average d-spacings of Stage IV, Stage III, Stage II, and Stage I were determined to be 3.42 Å (Figure 5I), 3.48 Å (Figure 5J), 3.54 Å (Figure 5K), and 3.70 Å (Figure 5L), respectively, which are consistent with those measured by the XRD (Figure 2 and Table S1). This suggests that each staged graphite exhibits long-range order and can be treated as a single-phase macroscopically. However, their local structure is complex and contains a series of defects, as displayed in Figures 4 and 5. For example, Defect I is present in Stage IV (top image of Figure 5E), where the interplanar spacing in the compressive region is 3.35 Å (top left image of Figure 5E) and 3.55 Å (top right image of Figure 5E) while that in the tensive region is 3.66 Å.

These results indicate that (1) Li ions intercalate into the graphite unevenly and localize at some regions, forming various staging structures concurrently at a specific lithiation state, (2) Defect I and II connect two different staging phases and help the phase transition between them even from the pristine graphite to the Stage I potentially by the diffusion of the Li ions as well as the movement and interact of the dislocations, and (3) the coexisting staging phases suggest that the macroscopically staged graphite is a mixture of various staging phases microscopically (Figure 5E–H), especially for the macroscopical Stage IV, Stage III, and Stage II. Therefore, the macroscopical Stage IV consists of the pristine graphite and differently staged

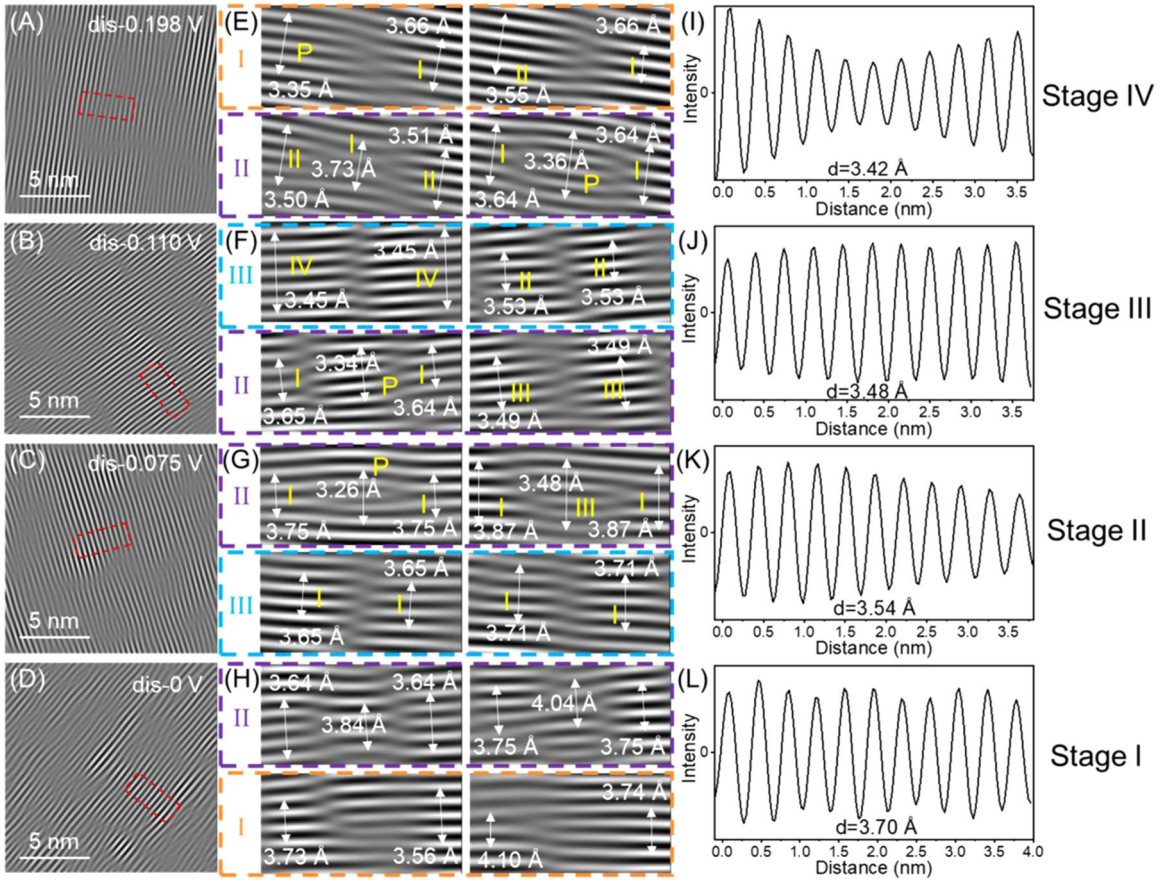

FIGURE 5 The long- and short-range structure of the lithiated graphite at different stages. (A–D) Cryo-transmission electron microscopy images, (E–H) representative defective structures with labeled d-spacing, (I–L) the line scan profiles of the 11 graphene layers along the red-marked region in (A–D) of Stage IV (A, E, and I), Stage III (B, F, and J), Stage II (C, G, and K), and Stage I (D, H, and L). dis, discharge.

GICs microscopically; the macroscopical Stage III is a combination of the Stage IV and Stage II as well as other staged phases in its microstructure; the macroscopical Stage II is a mixture of the Stage III and Stage I as well as other staged phases in its local structure. For the Stage I phase, as it is fully lithiated, there are few other staging phases present in the sample. However, its lattice is highly deformed and abundant in the dislocations, which divide the bulk into numbers of segments. Therefore, it is long-range order, medium-range disorder, and short-range order, which is different from the commonly believed order structural models proposed in the previous references (Figure 1).[14,15,32–34]

3.3 | Thermodynamic stability and dynamic transition of the staged graphite by density functional theory (DFT)

The thermodynamic stability of the lithiated graphite Li_xC_6 ($x = 0$, 1/4, 1/3, 1/2, and 1) at different stages was evaluated by the DFT calculation. The low formation energy (<50 meV/formula) of the Li_xC_6 ($x = 1/4$, 1/3, and 1/2) (Supporting Information: Figure S9) suggests that they are metastable based on the entropic effect[35] and are inclined to dismutate into other phases (dash line in Figure S9), such as from $Li_{1/3}C_6$ (LiC_{18}) to $Li_{1/4}C_6$ (LiC_{24}) and $Li_{1/2}C_6$ (LiC_{12}). This means that coexisting of the intermediate phases is energetically favorable. As dislocations and other defects were experimentally found in the lithiated graphite, artificial stacking faults and displacements were introduced into the initial structure models of Stage III as an example (Figure 6A–C). After structural relaxation, rumpling (Figure 6D), dislocation (Figure 6E), and Frank dislocation loop (Figure 6F) are present in the final structures, which is consistent with the Defect I–III observed by the above cryo-TEM (Figure 3). The formation of dislocations is related to the coexistence of the intermediate phases in which lattice mismatch causes local stress in the structure.

Ab initio molecular dynamics (AIMD) simulations were further carried out to explore the influence of these

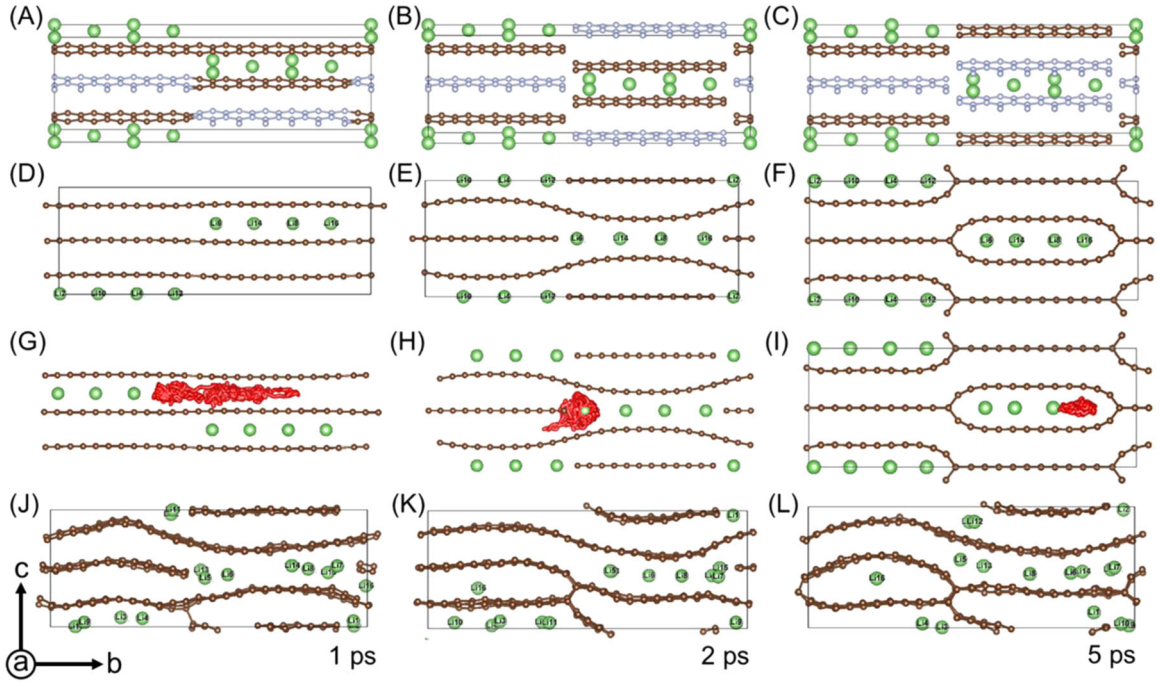

FIGURE 6 Structural simulation of Stage III (LiC_{18}). Three types of (A-C) initial and (D-F) relaxed structural configurations with various defects. (G–I) The Li-ion diffusion trajectory in the corresponding structures of (D–F) at 1000 K. (J–L) The structural evolution of the structure in (E) at 1, 2, and 5 ps during ab initio molecular dynamics simulation at 1500 K, respectively.

defects on the Li-ion diffusion and structural evolution (Figure 6G–I). The results show that Li ion near the defects can diffuse along the *c* axis (its trajectory is marked by red) smoothly apart from that in the Frank dislocation loop (Figure 6L) due to the strong repulsion of the C hexatomic ring. In addition, the dynamic structural evolution at 1500 K (Figure 6J–L and Movie S1, 1500 K is used to accelerate the atomic diffusion) shows the real-time diffusion of Li ions and their interplay with the defective structure. It is interesting to visualize the movement of graphene layers and the structural evolution through defect interaction. Therefore, a combination of Li-ion diffusion and defects interaction facilitates the phase transition between different stages.

3.4 | Discussion and applications

The above results illustrate a detailed structural evolution of the graphite during lithiation at the long-, medium-, and short-range scales (Figure 1). The intercalated Li ions distribute unevenly, generating local stress fields and dislocations in graphitic structures. Their content increases during lithiation and decreases during delithiation, demonstrating the highly reversible structural changes. These dislocations can move, interact, and interconvert, which facilitates the phase transition among different staged graphite.

For the structural nature of the staged graphite, it is ordered macroscopically and exhibits a long-range periodic arrangement with characteristic average interplanar distance and diffraction patterns. However, it is inhomogeneous microscopically and consists of different staging phases and dislocations. Therefore, it is long-range order, medium-range disorder, and short-range order, which is defined as the "Localized-domains" model (Figure 1C). This model is much different from the previously proposed Rüdorff-Hofmann (Figure 1A)[14] and Daumas-Hérold models (Figure 1B).[15]

The presence of the defective structure is found beneficial to reduce the energy barrier and facilitate the Li-ion diffusion across the graphite layers,[36] which enlightens to enhance the reaction kinetics of graphite through defect engineering. As a proof of concept, we artificially created some defects in the pristine graphite by mild KOH treatment and evaluated its rate performance for Li-ion storage (Figure 7). Although the high-resolution TEM (HRTEM) image shows that dislocations are present in a few layers of the graphite after KOH etching (Figure 7A, red rectangle), it dramatically increases the reversible capacity (Figure 7B) and capacity retention (Figure 7C) at the higher current density. At 400 mA g^{-1}, the KOH-etched graphite delivers a capacity of 335 mAh g^{-1} while it drops to 200 mAh g^{-1} for the pristine one (Figure 7B). When the cells were cycled at 800 mA g^{-1} for 150 cycles (Figure 7C, the capacity drop after 11 cycles was

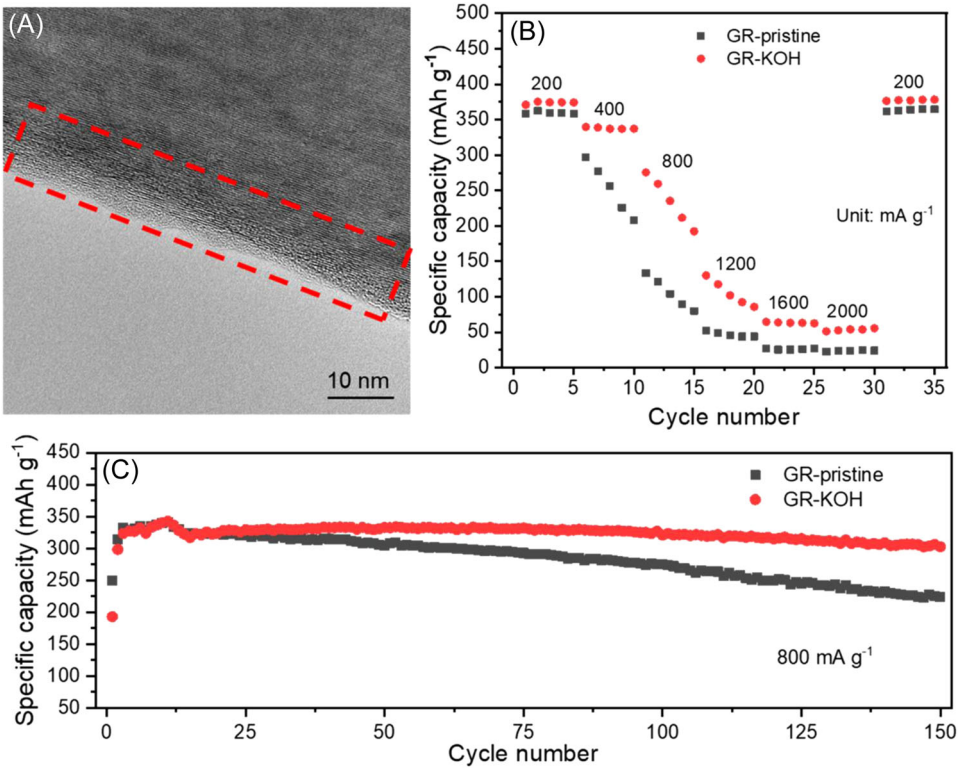

FIGURE 7 Performances of Li-ion intercalation/deintercalation in pristine graphite (black) and defective graphite (red). (A) The high-resolution transmission electron microscopy image of defective graphite. (B) Rate and cycling (C) performances. GR, graphite.

caused by temperature decrease), the former remains 300 mAh g^{-1} while the latter shows 224 mAh g^{-1}. These results unambiguously demonstrate the positive effect of defect engineering although mild on accelerating the transition kinetic among different staging structures and pave the way to improve the fast-charge capacity of graphite through tuning the local domains.

4 | CONCLUSION

Combining techniques sensitive to the long-range and local domains, we unraveled the nature of the staging structure and evolution of the lithium-intercalated graphite. The results show that the Li ions are intercalated unevenly, generating local stress and dislocations in the graphitic structure. A combination of Li-ion diffusion and dislocation interaction facilitates the transition among different staging phases. It is found that each staging compound is macroscopically ordered but microscopically inhomogeneous, and the transition of different staging structures can be improved by artificially increasing the concentration of the intrinsic defects. These findings renew the understanding of the structural nature of the lithiated graphite and the transition among different staging phases and provide suggestions on enhancing the reaction kinetic of layered materials in rechargeable batteries by defect engineering.

ACKNOWLEDGMENTS

The authors thank the financial support from the National Natural Science Foundation of China (NSFC nos. 52172257, 22005334, 21773301 and 52022106) and the Natural Science Foundation of Beijing (grant no. Z200013).

CONFLICTS OF INTEREST

The authors declare no conflicts of interest.

ORCID

Gaojing Yang http://orcid.org/0000-0002-9275-316X
Dong Su http://orcid.org/0000-0002-1921-6683
Xuefeng Wang http://orcid.org/0000-0001-9666-8942

REFERENCES

1. Laipanaipan M, Xiang L, Yu J, et al. Layered intercalation compounds: Mechanisms, new methodologies, and advanced applications. *Prog Mater Sci*. 2020;109:100631.
2. Dresselhaus MS, Dresselhaus G. Intercalation compounds of graphite. *Adv Phys*. 2002;51(1):1-186.
3. Hannay NB, Geballe TH, Matthias BT, Andres K, Schmidt P, MacNair D. Superconductivity in graphitic compounds. *Phys Rev Lett*. 1965;14(7):225-226.

4. Koike Y, Suematsu H, Higuchi K, Tanuma S. Superconductivity in graphite-alkali metal intercalation compounds. *Physica B+C*. 1980;99(1-4):503-508.
5. Zhao YY, Zhang YL, Wang Y, Cao DX, Sun X, Zhu HL. Versatile zero- to three-dimensional carbon for electrochemical energy storage. *Carbon Energy*. 2021;3(6):895-915.
6. Liu Q, Xu RG, Mu DB, et al. Progress in electrolyte and interface of hard carbon and graphite anode for sodium-ion battery. *Carbon Energy*. In press; doi:10.1002/cey2.120
7. Whittingham MS. *Intercalation Chemistry*. Academic Press; 1982.
8. Li YQ, Lu YX, Adelhelm P, Titirici MM, Hu YS. Intercalation chemistry of graphite: alkali metal ions and beyond. *Chem Soc Rev*. 2019;48(17):4655-4687.
9. Dresselhaus MS, Dresselhaus G. Intercalation compounds of graphite. *Adv Phys*. 1981;30(2):139-326.
10. Sha M, Liu L, Zhao HP, Lei Y. Anode materials for potassium-ion batteries: current status and prospects. *Carbon Energy*. 2020;2(3):350-369.
11. Gu L, Zhu C, Li H, et al. Direct observation of lithium staging in partially delithiated $LiFePO_4$ at atomic resolution. *J Am Chem Soc*. 2011;133(13):4661-4663.
12. Wang XF, Shen X, Wang ZX, Yu RC, Chen LQ. Atomic-scale clarification of structural transition of MoS_2 upon sodium intercalation. *ACS Nano*. 2014;8(11):11394-11400.
13. Huang Z, Hou Y, Wang T, et al. Manipulating anion intercalation enables a high-voltage aqueous dual ion battery. *Nat Commun*. 2021;2:3106.
14. Hofmann U, Rüdorff W. The formation of salts from graphite by strong acids. *Trans Faraday Soc*. 1938;34:1017-1021.
15. Daumas N, Herold A. Relations between phase concept and reaction mechanics in graphite insertion compounds. *C R Hebd Séances Acad Sci*. 1969;268(5):373-375.
16. Sole C, Drewett NE, Hardwick LJ. In situ Raman study of lithium-ion intercalation into microcrystalline graphite. *Faraday Discuss*. 2014;172:223-237.
17. Zheng T, Dahn JR. Effect of turbostratic disorder on the staging phase diagram of lithium-intercalated graphitic carbon hosts. *Phys Rev B*. 1996;53(6):3061-3071.
18. Wang X, Zhang M, Alvarado J, et al. New insights on the structure of electrochemically deposited lithium metal and its solid electrolyte interphases via cryogenic TEM. *Nano Lett*. 2017;17(12):7606-7612.
19. Wang XF, Li YJ, Meng YS. Cryogenic electron microscopy for characterizing and diagnosing batteries. *Joule*. 2018;2(11):2225-2234.
20. Li Y, Li Y, Pei A, et al. Atomic structure of sensitive battery materials and interfaces revealed by cryo-electron microscopy. *Science*. 2017;358(6362):506-510.
21. Shim JH, Lee SH. Characterization of graphite etched with potassium hydroxide and its application in fast-rechargeable lithium ion batteries. *J Power Sources*. 2016;324:475-483.
22. Cheng Q, Yuge R, Nakahara K, Tamura N, Miyamoto S. KOH etched graphite for fast chargeable lithium-ion batteries. *J Power Sources*. 2015;284:258-263.
23. Hÿtch MJ, Snoeck E, Kilaas R. Quantitative measurement of displacement and strain fields from HREM micrographs. *Ultramicroscopy*. 1998;74(3):131-146.
24. Kresse G, Furthmüller J. Efficiency of ab-initio total energy calculations for metals and semiconductors using a plane-wave basis set. *Comput Mater Sci*. 1996;6(1):15-50.
25. Blöchl PE. Projector augmented-wave method. *Phys Rev B*. 1994;50(24):17953-17979.
26. Perdew JP, Burke K, Ernzerhof M. Generalized gradient approximation made simple. *Phys Rev Lett*. 1996;77(18):3865-3868.
27. Nosé S. A unified formulation of the constant temperature molecular dynamics methods. *J Chem Phys*. 1984;81(1):511-519.
28. He Y, Liu Z, Zhou G, et al. Dislocation dipole-induced strengthening in intermetallic TiAl. *Scr Mater*. 2018;143:98-102.
29. Gottstein G. *Physical Foundations of Materials Science*. Springer Science & Business Media; 2013.
30. Song HB, Xie HM, Xu CC, Kang YL, Li CW, Zhang Q. In situ measurement of strain evolution in the graphene electrode during electrochemical lithiation and delithiation. *J Phys Chem C*. 2019;123(31):18861-18869.
31. Yadegari H, Koronfel MA, Wang K, et al. Operando measurement of layer breathing modes in lithiated graphite. *ACS Energy Lett*. 2021;6(4):1633-1638.
32. Matsunaga T, Takagi S, Shimoda K, et al. Comprehensive elucidation of crystal structures of lithium-intercalated graphite. *Carbon*. 2019;142:513-517.
33. Didier C, Pang WK, Guo Z, Schmid S, Peterson VK. Phase evolution and intermittent disorder in electrochemically lithiated graphite determined using in operando Neutron diffraction. *Chem Mater*. 2020;32(6):2518-2531.
34. Li N, Su D. In-situ structural characterizations of electrochemical intercalation of graphite compounds. *Carbon Energy*. 2019;1(2):200-218.
35. Hong YL, Liu Z, Wang L, et al. Chemical vapor deposition of layered two-dimensional $MoSi_2N_4$ materials. *Science*. 2020;369(6504):670-674.
36. Yang G, Liu Z, Weng S, et al. Iron carbide allured lithium metal storage in carbon nanotube cavities. *Energy Storage Mater*. 2021;36:459-465.

SUPPORTING INFORMATION

Additional supporting information can be found online in the Supporting Information section at the end of this article.

How to cite this article: Weng S, Wu S, Liu Z, et al. Localized-domains staging structure and evolution in lithiated graphite. *Carbon Energy*. 2022;1-10. doi:10.1002/cey2.224